Acta of Bioengineering and Biomechanics
Vol. 17, No. 2, 2015

Original paper
DOI: 10.5277/ABB-00073-2014-03

A numerical study on indentation properties of cortical bone tissue: Influence of anisotropy

MURAT DEMIRAL[1], ADEL ABDEL-WAHAB[2], VADIM SILBERSCHMIDT[2]*

[1] Department of Mechanical Engineering, University of Turkish Aeronautical Association, 06790 Ankara, Turkey.
[2] Wolfson School of Mechanical and Manufacturing Engineering, Loughborough University, LE11 3TU, UK.

Purpose: The purpose of this study is to investigate the effect of anisotropy of cortical bone tissue on measurement of properties such as direction-dependent moduli and hardness. Methods: An advanced three-dimensional finite element model of micro-indentation was developed. Different modelling schemes were considered to account for anisotropy of elastic or/and plastic regimes. The elastic anisotropic behaviour was modelled employing an elasticity tensor, and Hill's criteria were used to represent the direction-dependent post-yield behaviour. The Oliver–Pharr method was used in the data analysis. Results: A decrease in the value of the transverse elasticity modulus resulted in the increased material's indentation modulus measured in the longitudinal direction and a decreased one in the transverse direction, while they were insensitive to the anisotropy in post-elastic regime. On the other hand, an increase in plastic anisotropy led to a decrease in measured hardness for both directions, but by a larger amount in the transverse one. The size effect phenomenon was found to be also sensitive to anisotropy. Conclusions: The undertaken analysis suggests that the Oliver–Pharr method is a useful tool for first-order approximations in the analysis of mechanical properties of anisotropic materials similar to cortical bone, but not necessarily for the materials with low hardening reserves in the plastic regime.

Key words: *finite element analysis, anisotropy, Oliver–Pharr method, cortical bone tissue, indentation*

1. Introduction

Bone with its hierarchical structure has distinct microstructures at different length scales. Cortical bone tissue (CBT), for instance, at micro-scale level (500 μm to 1 μm) consists of interstitial matrix, long cylindrical fibres, known as osteons, cement lines and lamellae. At nano-scale level (1 μm to 1 nm) collagen fibrils, collagen and non-collagenous proteins are the main constituents. The effective, continuum properties of bone at a sub-millimetre scale are governed by the properties of its constituents at lower length scales [17]. To predict its behaviour under real-life deformations [15], mechanical properties of such micro-constituents are required.

Micro- or nano-indentation is a widely used experimental technique to determine mechanical properties of thin films, small volumes and small microstructural features at micron scales [5]. This technique has been applied to the measurement of mechanical properties of biomaterials including bone [10]. However, elasticity and plasticity in bone and its micro-constituents are complicated by their anisotropic features. The extent of anisotropy varies significantly for different bone types, hierarchical levels and other factors such as age, injury or disease [7]. For instance, for cortical bone, the nano-

* Corresponding author: Vadim Silberschmidt, Wolfson School of Mechanical and Manufacturing Engineering, Loughborough University, LE11 3TU Loughborough, United Kingdom. Tel: ++44 1509 227 504, e-mail: V.Silberschmidt@lboro.ac.uk
Received: April 4th, 2014
Accepted for publication: August 8th, 2014

indentation-based values of elastic modulus of interstitial matrix and osteons in the longitudinal direction, 25.7 and 22.4 GPa, respectively, are larger than those in the transverse direction – 16.6 GPa (considered to be the same for both constituents). This means the anisotropy ratio (defined here as the ratio of a longitudinal parameter to a transvers one) of 1.54 and 1.35, respectively [21]. Rho and Pharr reported this value to be 1.29 for the trabecular bone, which differs significantly from that of macroscopic wet femoral cortical specimens, 1.77 [20]. This correlates well with the data on anisotropy levels obtained experimentally on macroscopic specimens for various cortices of a bovine femur – from 1.35 (for a lateral cortex) to 1.94 (for a posterior one) [1]. On the other hand, Liu et al. [16] reported osteonal bone to be less anisotropic with a value of 1.33. This was linked to the fact that mineralized collagen fibrils in osteonal bone bundle into layers with varying directions to form a plywood-like structure unit in addition to rotation about their axes within these layers [26]. Anisotropy of the post-yield regime is respectively less explored. Only Rho et al. [21], Wang et al. [25] and Carnelli et al. [6] studied direction-dependency of material's plastic behaviour.

The objective of this study is to investigate the influence of material's anisotropy of elastic or/and plastic regimes on direction-dependent properties of cortical bone obtained by means of indentation such as elastic moduli and hardness as well as to study the size effect phenomenon. To achieve this, a three-dimensional finite element model of micro-indentation was developed. It should be emphasized that numerical simulations enable elucidation of complex deformation mechanisms in the indentation zone affected by complicated boundary and kinematic conditions, microstructural size effects, anisotropy and heterogeneity of strain and stress fields [27]. Finite-element analysis provides deeper insights into structural and mechanical features of the tested material and underpinning deformation mechanisms [19]. In the developed FE model, elastic anisotropic behaviour was modelled employing an elasticity tensor, and Hill's criteria were used to represent the direction-dependent post-yield behaviour. The Oliver–Pharr method was used in the data analysis. Various hardening models of the post-yield deformation regime representing different material behaviours were considered to assess the effect of anisotropy on the indentation properties and underlying deformation mechanisms for materials other than bone.

2. Materials and Methods

2.1. Modelling considerations

To obtain a thorough understanding of various material models with different anisotropic ratios (*AR*) of elastic or/and plastic regimes, four different finite-element models were developed to implement a comparative analysis of numerical results. The indentation process for each modelling regime was studied for the same magnitude of the maximum indentation depth into a target made of the material under study, reflecting conditions of a micro-indentation test.

First, an isotropic material model was considered (referred to as type I), a scheme that has been traditionally used to simulate conventional indentation tests. Additionally, three anisotropic material models were studied: the first one represents anisotropy in both elastic and plastic regimes (type A); the second is characterised by elastic anisotropy while plasticity is considered isotropic (type B); the third assumes anisotropy in the plastic regime only, with isotropic elasticity (type C). In all the modelling schemes – apart from type I – the effect of the extent of anisotropy on the obtained mechanical properties was investigated by considering two different levels of *AR* to values, 1.25 and 1.67. A summary of the material models used in the various modelling scenarios is listed in Table 1. In the next Section, the Oliver–Pharr (O-P) method is summarized.

Table 1. Anisotropy ratios (*AR*) for different modelling schemes

Material model	I	A1	A2	B1	B2	C1	C2
Elastic	I	1.25	1.67	1.25	1.67	1.0	1.0
Plastic	I	1.25	1.67	1.0	1.0	1.25	1.67

2.2. Oliver–Pharr method

The Oliver–Pharr (O-P) method was originally developed to measure the mechanical properties of elasto-plastic materials using depth-sensitive indentation with sharp indenters [18]. This method can also be applied in any axi-symmetrical indenter geometries such as a spherical one [14], [18]. The O-P technique was developed employing the as-

sumption that the indented material possesses homogeneous and isotropic properties. The details of this technique including its advantages compared to other methods can be found in [18]. In fact, the precision of the O-P method significantly depends on accuracy of measurement of a contact area. Therefore, the exactness of definition of the contact area can be considered as a criterion for assessment of closeness of the obtained numerical solutions to this method. Fan and Rho [10] compared the accuracy of contact areas using the O-P method for different material models. It was observed that the O-P method gave a better estimation for the models with higher strain-hardening reserves.

In the Oliver–Pharr method, the elastic modulus is calculated from the unloading curve, based on the assumption that it is unaffected by inelastic phenomena. Equation (1) was used to fit the top 40% of the unloading curve, where P is the load applied to the indenter, h_f is the residual depth after unloading and B and m are the fitting parameters. The indentation modulus E_r is calculated using equation (2), where S is contact stiffness corresponding to the slope of indentation unloading curve at the maximum indentation depth (h_{max}) (equation (3)) and A_p is the projected contact area calculated at h_{max}. A_p can be obtained from the known value of the contact area (A) using geometry of the indenter. Apparently, equation (2) is derived based on the assumption that the material is homogeneous and isotropic elastically. However, in an anisotropic material, the obtained modulus corresponds to the average of the anisotropic elastic constants biased towards the modulus in the direction of loading [21]. The expression for the elastic moduli of the specimen (E) in equation (4) is obtained from the assumption that the indenter is a rigid body as its elastic modulus (E_i) is much larger than that of the specimen.

$$P = B\,(h - h_f)^m, \tag{1}$$

$$E_r = \frac{\sqrt{\pi}}{2}\frac{S}{\sqrt{A_p}}, \tag{2}$$

$$S = \left(\frac{dP}{dh}\right)_{h_{max}} = Bm(h - h_f)^{m-1}, \tag{3}$$

$$E = (1-\upsilon^2)\frac{\sqrt{\pi}}{2}\frac{S}{\sqrt{A_p}}, \quad \frac{1}{E_r} = \frac{1-\upsilon^2}{E} + \frac{1-\upsilon_i^2}{E_i}, \tag{4}$$

$$H = \frac{P_{max}}{A_p}, \tag{5}$$

$$A_{p\text{-}OP} = \pi h_c(2R - h_c), \quad h_c = h_{max} - \varepsilon_g\frac{P_{max}}{S}. \tag{6}$$

Hardness (H) is calculated using equation (5), where P_{max} is the maximum load at h_{max}. The projected contact area using the O-P method, hereafter denoted $A_{p\text{-}OP}$, is calculated using equation (6), where R corresponds to radius of the spherical indenter, h_c is the contact depth and ε_g is the geometrical parameter. The main disadvantage of the O-P method is that it does not take into account the pile-up height in calculation of A; thus, this value is underestimated. To quantify this deviation from its true value, A is computed here using also the FE simulations accounting for the pile-up height. In the simulations described the Abaqus output variable COPEN (contact opening distance) with a threshold value of 10^{-5} was used to define the boundary of the contact [23], where the area within the boundary (A) was computed employing Plot Digitizer 2.4.1 [12]. The corresponding projected contact area is denoted $A_{p\text{-}FE}$ here.

2.3. Finite-element modelling of nano-indentation experiment

A schematic of the developed indentation model is shown in Fig. 1. Dimensions of the workpiece used in the FE model were 250 μm × 250 μm × 250 μm. A refined mesh with a characteristic element size of 400 nm in the vicinity of the indenter's tip and a coarser mesh for the remaining domain were used to discretize the workpiece sample, resulting in 53488 eight-node linear brick elements (C3D8) in total (Fig. 1a). The spherical indenter used in the simulations was modelled as a rigid body since its modulus is much higher than that of bone; its geometrical parameter ε_g = 0.75 [18]. The relative movement of the workpiece and indenter was monitored by translation of the latter in the negative z-direction for longitudinal tests with a maximum indentation depth of 2.0 μm followed by a complete unloading. Kinematic boundary conditions were imposed on the bottom face of the workpiece by constraining displacements in all directions, whereas its faces perpendicular to x- and y-directions were constrained in x- and y-direc-

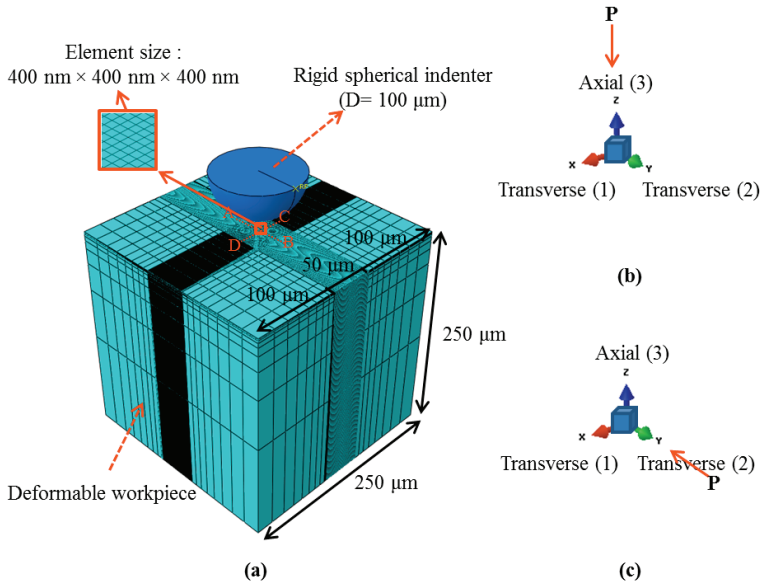

Fig. 1. (a) 3D finite-element model of micro-indentation; schematic representation of axial (b) and transverse indentation (c) (arrow P demonstrates direction of indentation)

tion, The Coulomb's friction law was used to model fric-tional interaction between the indenter and the surface of the workpiece material. It should be noted that frictionless contact conditions were considered in the simulations unless stated otherwise. As large displacements and rotations are intrinsic to indentation, the large-deformation theory was used. The simulations were performed using the commercial FE code Abaqus/Standard [23]. Each model requires on average 8 h on 12 Intel quad-core processors with 48 GB RAM each to finish the analysis using High Performance Computing (HPC) facility available at Loughborough University.

In this study, all the anisotropic material models were assumed to be transversely isotropic, i.e., identical properties in the directions perpendicular to the longitudinal axis with different properties on it (Fig. 1(b)); this is a reasonable approximation for the cortical bone tissue. Here, it is assumed that 1-2 plane is the plane of isotropy at every point in defining transversely isotropic elasticity. Then, $E_1 = E_2 = E_T$, $E_3 = E_L$, $G_{13} = G_{23} = G_{LT}$ and $G_{12} = G_{TT}$ can be written, where T and L stand for "transverse" and "longitudinal" (or axial), respectively. The schematic representations of the axial and transverse indentations are presented in Fig. 1(b) and Fig. 1(c), respectively. The stress-strain law for such a transversely isotropic material in the elastic region can be written as follows

$$\begin{Bmatrix} \varepsilon_{11} \\ \varepsilon_{22} \\ \varepsilon_{33} \\ \gamma_{12} \\ \gamma_{13} \\ \gamma_{23} \end{Bmatrix} = \begin{bmatrix} 1/E_T & -\vartheta/E_T & -\vartheta/E_L & 0 & 0 & 0 \\ -\vartheta/E_T & 1/E_T & -\vartheta/E_L & 0 & 0 & 0 \\ -\vartheta/E_T & -\vartheta/E_T & 1/E_L & 0 & 0 & 0 \\ 0 & 0 & 0 & 1/G_{TT} & 0 & 0 \\ 0 & 0 & 0 & 0 & 1/G_{LT} & 0 \\ 0 & 0 & 0 & 0 & 0 & 1/G_{LT} \end{bmatrix} \begin{Bmatrix} \sigma_{11} \\ \sigma_{22} \\ \sigma_{33} \\ \sigma_{12} \\ \sigma_{13} \\ \sigma_{23} \end{Bmatrix}, \tag{7}$$

where $G_{TT} = E_T/2(1+\upsilon)$ and it is assumed that $G_{LT} = G_{TT}AR$. In this study, Poisson's ratio (υ) in all directions is assumed to be the same [17] in order to eliminate its influence on the numerical results obtained. Therefore, the total number of independent elasticity constants in equation (7) reduces to 4.

Anisotropic plasticity, characterised by different yield behaviours in different indentation directions, was introduced employing user-defined stress ratios that were applied in the Hill's potential function. This model assumes symmetry in tension and compression yield stresses. The mathematical form of this potential is reviewed below.

The Hill's potential function for 3D stresses involves six anisotropy parameters – F, G, H, L, M, N – obtained by tests of the material in different orientations, and can be expressed with respect to its orthotropy axes (e_1, e_2, e_3) as follows

$$f(\sigma)=\sqrt{F(\sigma_{22}-\sigma_{33})^2+G(\sigma_{33}-\sigma_{11})^2+H(\sigma_{11}-\sigma_{22})^2+2L\sigma_{23}^2+2M\sigma_{31}^2+2N\sigma_{12}^2}\,, \tag{8}$$

where

$$F=\frac{(\sigma^0)^2}{2}\left(\frac{1}{\bar{\sigma}_{22}^2}+\frac{1}{\bar{\sigma}_{33}^2}-\frac{1}{\bar{\sigma}_{11}^2}\right)=\frac{1}{2}\left(\frac{1}{R_{22}^2}+\frac{1}{R_{33}^2}-\frac{1}{R_{11}^2}\right),$$

$$G=\frac{(\sigma^0)^2}{2}\left(\frac{1}{\bar{\sigma}_{33}^2}+\frac{1}{\bar{\sigma}_{11}^2}-\frac{1}{\bar{\sigma}_{22}^2}\right)=\frac{1}{2}\left(\frac{1}{R_{33}^2}+\frac{1}{R_{11}^2}-\frac{1}{R_{22}^2}\right), \tag{9}$$

$$H=\frac{(\sigma^0)^2}{2}\left(\frac{1}{\bar{\sigma}_{11}^2}+\frac{1}{\bar{\sigma}_{22}^2}-\frac{1}{\bar{\sigma}_{33}^2}\right)=\frac{1}{2}\left(\frac{1}{R_{11}^2}+\frac{1}{R_{22}^2}-\frac{1}{R_{33}^2}\right),$$

$$L=\frac{3}{2}\left(\frac{\tau^0}{\bar{\sigma}_{23}}\right)^2=\frac{3}{2R_{23}^2},\quad M=\frac{3}{2}\left(\frac{\tau^0}{\bar{\sigma}_{13}}\right)^2=\frac{3}{2R_{13}^2},$$

$$N=\frac{3}{2}\left(\frac{\tau^0}{\bar{\sigma}_{12}}\right)^2=\frac{3}{2R_{12}^2}.$$

$\bar{\sigma}_{ij}$ is the measured yield stress value upon σ_{ij} applied as the only nonzero stress component in a certain direction, σ^0 is the user-defined reference yield stress, τ^0 is equal to $\sigma^0/\sqrt{3}$, and R_{ij} are anisotropic yield stress ratios through which anisotropic yield was introduced, where they are defined as follows

$$R_{11}=\frac{\bar{\sigma}_{11}}{\sigma^0},\quad R_{22}=\frac{\bar{\sigma}_{22}}{\sigma^0},\quad R_{33}=\frac{\bar{\sigma}_{33}}{\sigma^0},\quad R_{12}=\frac{\bar{\sigma}_{12}}{\tau^0},$$

$$R_{13}=\frac{\bar{\sigma}_{13}}{\tau^0},\quad R_{23}=\frac{\bar{\sigma}_{23}}{\tau^0}. \tag{10}$$

In this study, as σ^0 was assigned to the yield stress in the axial (longitudinal) direction, i.e., R_{33} = 1. It was assumed that the shear yield stresses in the longitudinal-transverse plane ($\bar{\sigma}_{13}$, $\bar{\sigma}_{23}$) equals τ^0, thus, R_{13} = R_{23} = 1, whereas R_{12} = 1/AR. The elastic and plastic constants used in the simulations are presented in Table 2.

To represent the post-yield behaviour for the reference stress σ^0, the model based on the experiments in [2] was considered (Fig. 2). In this model the maximum available plastic strain was limited to ~ 5% due to unavailability of the data for larger strain values.

Table 2. Elastic and yield parameters of cortica bone tissue [2] adopted in simulations

Elastic constants		Plastic constants	
$E_1 = E_2$ (MPa)	18000/AR	$R_{11} = R_{22}$	1/AR
E_3 (MPa)	18000	R_{33}	1
ν_{ij}, i, j = 1, 2, 3	0.30	R_{12}	1/AR
G_{12} (MPa)	5384.60/AR	$R_{13} = R_{23}$	1
$G_{13} = G_{23}$ (MPa)	5384.60		

However, it was significantly less than the strain values, which the workpiece material experience during deformation, especially in the vicinity of the indenter's tip, ~ 50–60%. As Abaqus [23] assumes stress value to be constant outside the specified range of plastic strain value, this model (denoted X in Fig. 2) represented a perfect-plasticity regime beyond ~ 5% strain in the simulations. Our first FE results, based on this model, demonstrated that some amount of pile-up with a maximum value of 155.76 nm occurred around the indent. Fan and Rho [10] using atomic force microscopy (AFM) showed that a pile-up rarely occurred in indentation of cortical bone tissue. To represent its behaviour more adequately, we considered another plastic model with strain-hardening acting along the whole range of plastic strain (labelled "Present" in Fig. 2). It was found that the pile-ups were diminished reasonably in simulations with this model (maximum pile-up height is 104.10 nm), representing the post-yield behaviour of the CBT more accurately and, hence, was used in the subsequent simulations.

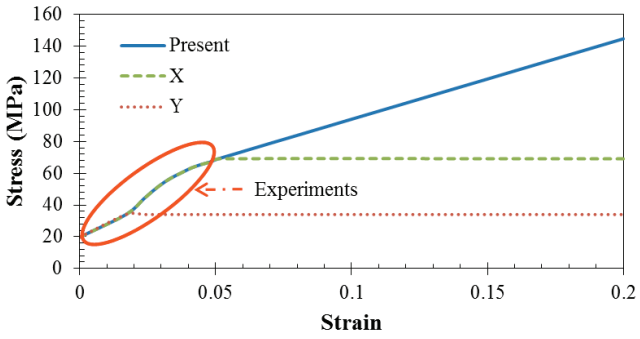

Fig. 2. Stress–strain relationships for different material models

3. Results

In this Section, we evaluate different parameters such as force-displacement curves, elastic moduli, hardness and strain gradients for different modelling schemes.

3.1. Force-displacement curve and elastic modulus

First of all, the effect of material model was evaluated for different combinations of elastic and plastic anisotropy ratios by comparing the shape of the simulated force-displacement (*F-d*) curves. Fig. 3(a), (c), (e) and Fig. 3(b), (d), (f) demonstrate the loading–unloading curves calculated for indentation along the longitudinal and transverse directions for different modelling schemes, respectively. Apparently, as the extent of anisotropy (value of *AR*) was changed by keeping the parameters in the longitudinal direction constant and varying the respective values in the transverse directions, the influence of *AR* on the *F-d* curves is larger for the latter direction as seen from the comparison of Fig. 3(a) and Fig. 3(b).

Figure 3(c) demonstrates that a change in the value of *AR* for elasticity does not affect the *F-d* curve for axial indentation significantly, whereas, an appreciable variation is observed when anisotropy of plasticity was changed (Fig. 3(e)). Similar observations can be made for indentations in transverse direction by comparing Fig. 3(d) and Fig. 3(f). This can be explained by the fact that deformation in indentation is largely a plastic one and contribution of elastic component is limited.

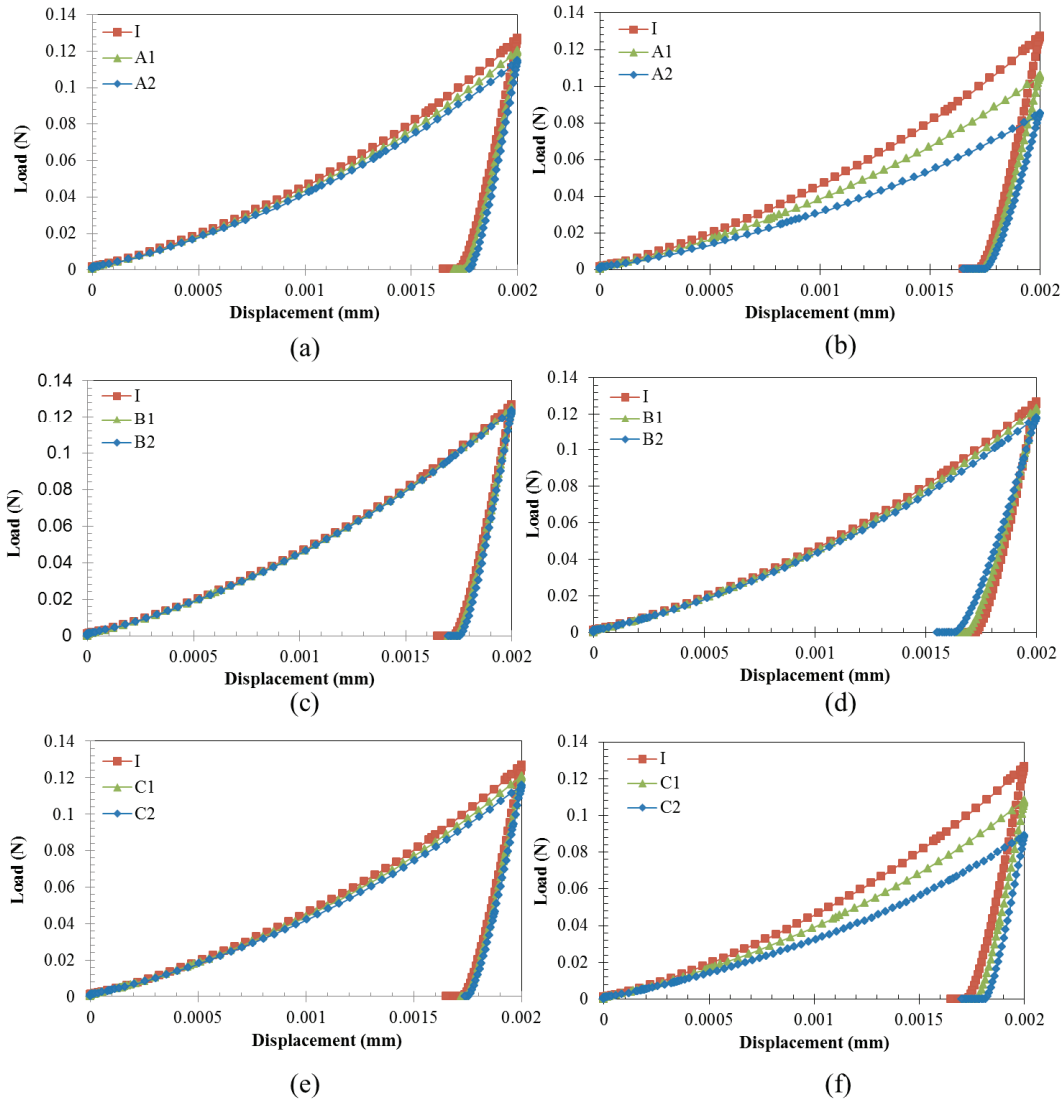

Fig. 3. Load-displacement curves for indentation along longitudinal (a, c, e) and transverse directions (b, d, f) of CBT for different modelling schemes

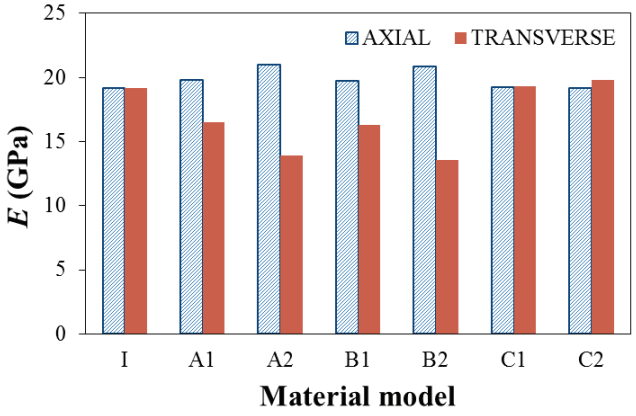

Fig. 4. Elastic moduli of CBT obtained from FE simulations of indentation in both axial and transverse directions for different material models

Figure 4 presents the calculated magnitudes of the specimen's elastic modulus. An important observation is that when the value of *AR* of elasticity increased, i.e., *AR* was changed from 1.25 to 1.67 (in models A and B), *E* decreased in the transverse direction from 16.5 GPa to 13.9 GPa and from 16.3 GPa to 13.5 GPa, respectively; whereas it increased in the longitudinal direction from 19.8 GPa to 21.0 GPa (model A) and from 19.7 GPa to 20.8 GPa (model B). This, in turn, led to an increase in the anisotropy ratio for Young's modulus, with approx. values of 1.51 and 1.56 for models A2 and B2, respectively. These results demonstrate that with a decrease in the elasticity modulus in the transverse direction the material's indentation modulus increases in the longitudinal direction and decreases in the transverse one. On the other hand, *E* values in model C were found to be very close to each other, with an average value of 19.4 MPa (Fig. 4), proving the fact that anisotropy in plasticity does not influence the indentation modulus significantly.

3.2. Hardness

Hardness is the resistance of a material to plastic deformation. To describe its change appropriately for different material formulations, firstly the influence of *AR* on the projected contact area was investigated in detail as A_p is one of the parameters in calculating *H* (equation (5)).

It is well known that materials around the contact area usually deform and do not remain flat; instead, they flow upwards (pile-up) or downwards (sink-in), which, in turn, causes the contact area to be larger or smaller, respectively, compared to the cross-sectional area of the indenter [24]. Figure 5(a) demonstrates a profile of the 3D surface of the workpiece material at maximum loading in the transverse direction analysed with model C2. As the properties in the respective transverse directions (directions 1 and 3, Fig. 1(c)) were different, the pile-up heights on those axes were found to vary, resulting in a contact periphery to be elliptical rather than circular (Fig. 5(b)), as in the case of axial direction.

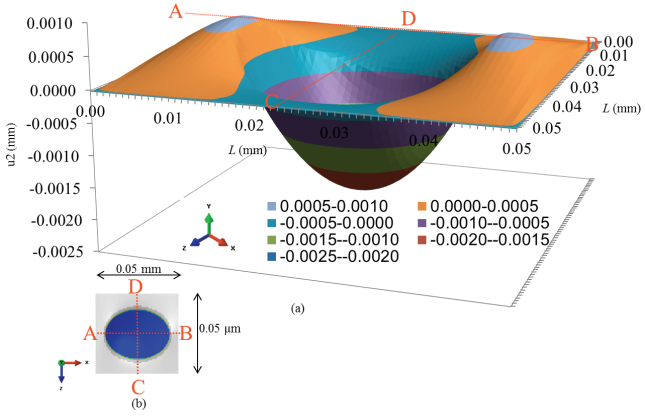

Fig. 5. (a) 3D surface topography of indented surface at maximum loading formed by indentation in transverse direction with model C2; (b) respective contact surface

The pile-up profiles of the indented surface along paths A-B and C-D for different *AR* for models B and C in the indentation of transverse direction are compared in Fig. 6. It was observed that with an increase in the value of *AR* for elasticity, the pile-up height decreased slightly on both paths (Fig. 6(a), (b)), whereas, with an increase in the value of *AR* for plasticity, this height increased significantly on path A-B (Fig. 6(c)), but decreased significantly on path C-D (Fig. 6(d)). The comparison between Fig. 6(a), (b) and Fig. 6(c), (d) also demonstrates that the pile-up profile is more sensitive to variation in anisotropy of plasticity than that of elasticity. The corresponding pile-up profiles in axial indentation are shown in Fig. 7. It was observed that with a change in *AR*, the pile-up height did not change considerably.

Table 3 presents different projected contact area values including their difference (in per cent) for the material models used. Obviously, for all the models the value of $A_{p\text{-}FE}$ is significantly larger than that of $A_{p\text{-}OP}$. The obvious reason is that the latter neglects the piling-up of the material [18]. It was also observed that the variation in the value of *AR* caused a greater change in the obtained A_p value in the transverse direction compared to that for the axial one. For instance, a transition from model I to A2 resulted in the increased relative difference – from 10.7% to 13.1% in transverse direction, whereas this parameter decreased only to 9.3% in axial direction.

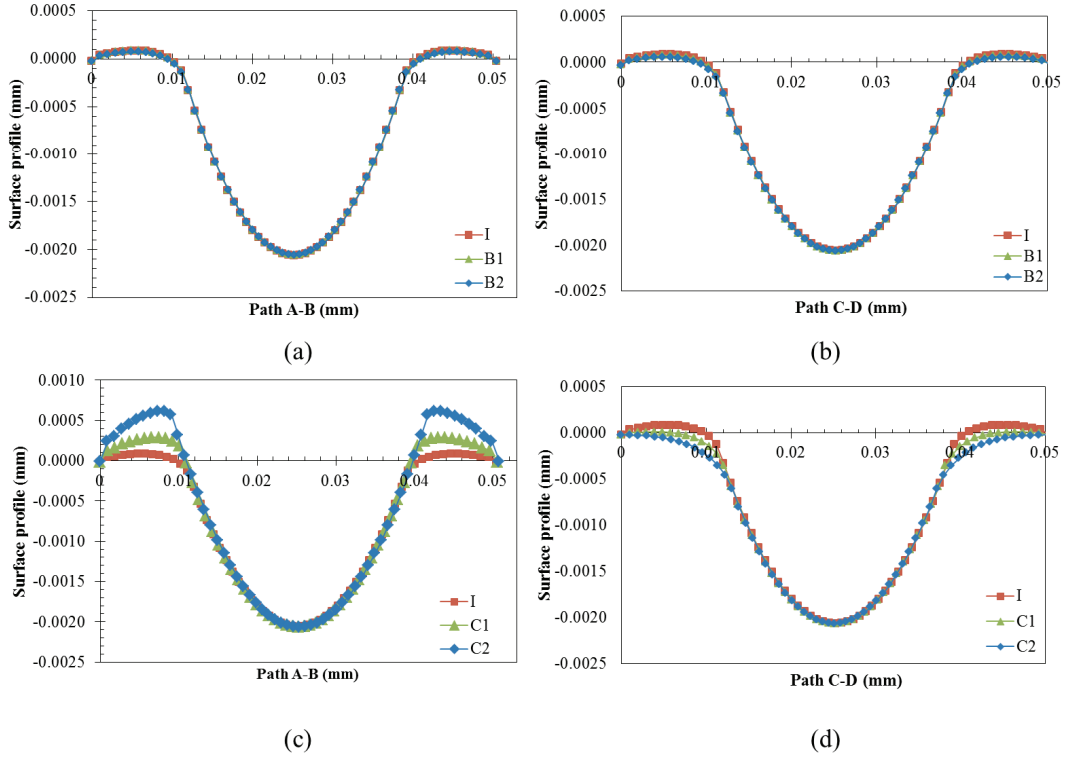

Fig. 6. Pile-up profiles of indented surfaces along paths A-B (a), (c) and C-D (b), (d) at maximum loading from indentation in transverse direction for models I, B and C

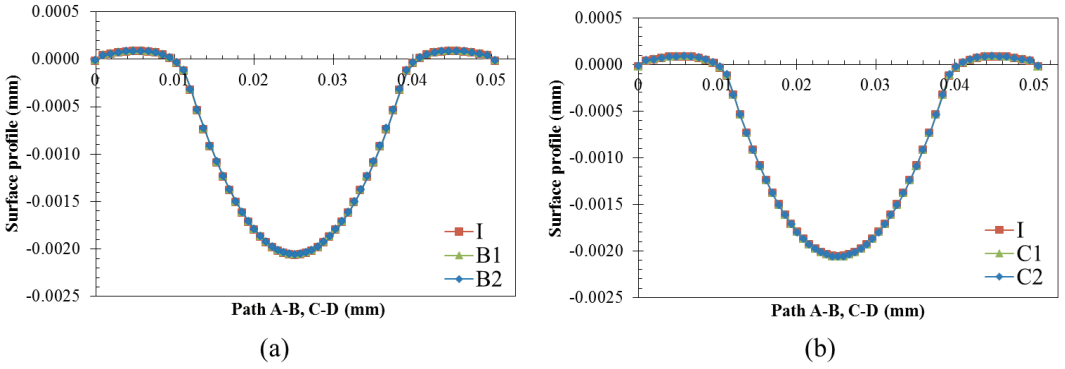

Fig. 7. Pile-up profiles of indented surfaces along paths A-B and C-D at maximum loading from indentation in axial direction for models I, B and C

In this study, the accuracy of the O-P method was analysed for different model parameters such as different hardening reserves and contact conditions. The post-yield behaviour for the reference stress σ^0 was compared for the existing hardening model with the model Y demonstrated in Fig. 2 that is characterised by negligibly small hardening reserves (nearly an elastic-ideal-plastic behaviour) for the modelling scheme I. It was observed that model Y led to a significant increase in the amount of piling-up around the indent with a maximum value of 550.3 nm, which, in turn, was a reason for the O-P method to give a poor estimation for the A_p value with a deviation of 26.0% from its value obtained with FE simulations (Table 4).

The influence of friction on the obtained numerical results was also investigated. Four different values of the coefficient of friction – 0.0 (as in the above simulations), 0.1, 0.2 and 0.4 – were used in the simulations. Obviously, $\mu = 0.0$ represents an idealized frictionless condition, considered as an extreme case of friction reduction due to perfect lubrication, while $\mu = 0.4$ accounts for significant friction, e.g., a lack of lubrication. Table 4 presents the difference between $A_{p\text{-}OP}$ and $A_{p\text{-}FE}$ as well as the pile-up height at maximum indentation loading for different μ values and

Table 3. Comparison between A_{p-OP} and A_{p-FE} at maximum loading for different models

Model	A_{p-OP} (μm^2)	A_{p-FE} (μm^2)	$(A_{p-FE} - A_{p-OP})/A_{p-FE}$ (%)
Axial			
I	567.8	636.1	10.7
A1	571.8	636.8	10.2
A2	576.3	635.6	9.3
B1	569.6	633.4	10.1
B2	572.5	631.9	9.4
C1	570.2	638.4	10.7
C2	572.0	639.4	10.5
Transverse			
I	567.8	636.1	10.7
A1	569.8	650.3	12.4
A2	572.4	659.0	13.1
B1	560.6	629.1	10.9
B2	551.8	623.5	11.5
C1	575.7	653.5	11.9
C2	583.9	669.3	12.8

hardening models for model I. It was observed that with an increase in the coefficient of friction from 0 to 0.4, the difference between the values of A_p obtained with the O-P method and FE analysis reduced from 26.0% to 20.6% for model Y, whereas a slight change, from 10.7% to 10.2%, was found for the present hardening model. Clearly, frictional effects are more important for the model with low strain-hardening, where there is a strong tendency of piling up around the indent. The pile-up was diminished in the strain-hardening model due to the fact that localized hardening near the contact periphery impedes plasticity in the sub-surface layers, which, in turn, drives the plastic zone deeper into the material rather than radially outwards [13], [24]. It was also found that an increase in the value of μ from 0.0 to 0.2 influenced the pile-up height and, hence, influenced the difference between the A_{p-OP} and A_{p-FE}. A further increase in μ did not cause any additional reduction in the material's pile-up due to the fact that nonslip contact conditions were already reached at $\mu = 0.2$.

Table 4. Comparison between A_{p-OP} and A_{p-FE} at maximum loading for different material models and contact conditions in model I with respective maximum pile-up heights (in brackets)

Material model	$\mu = 0.0$	$\mu = 0.1$	$\mu = 0.2$	$\mu = 0.4$
Present	10.7% (104.1 nm)	10.5% (102.7 nm)	10.3% (99.7 nm)	10.2% (97.6 nm)
Y	26.0% (550.3 nm)	22.0% (375.8 nm)	20.8% (331.2 nm)	20.6% (323.0 nm)

Having studied extensively the effect of various model parameters on the projected contact area, the next stage of analysis is linked with assessing hardness for different material model. It should be emphasized that A_{p-FE} was used in calculations of hardness in equation (5). As H represents material's resistance to plastic deformation, the variation in the value of AR for elasticity, represented in model B did not change the calculated values significantly for both indentation directions (Fig. 8). This explains also the reason for the similarity of the trends of H in models A and C. On the other hand, an increase in AR for plasticity, represented in model C, led to a decrease in H in both directions, but by a larger amount in the transverse one. It was demonstrated before that such a change led to the decrease in the obtained level of P_{max} (Fig. 3(f)) and an increase in A_{p-FE} in transverse indentation (Table 3), which, in turn, led to a natural decrease in H. However, such a decrease in axial indentation resulted in a smaller diminishment in P_{max} (Fig. 3(e)) without any substantial change in A_{p-FE} (Table 3); thus, a smaller drop in H was observed.

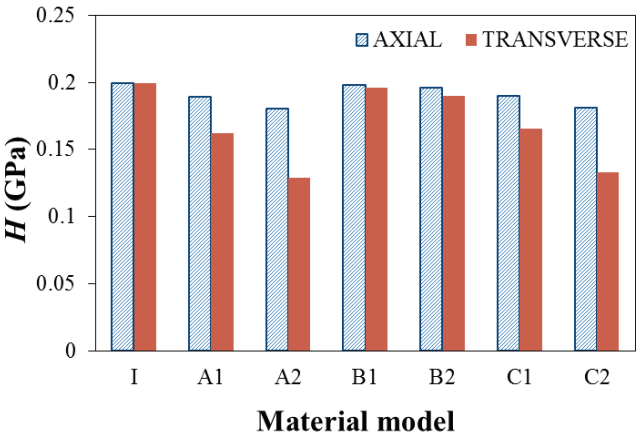

Fig. 8. Hardness of CBT obtained with FE simulations of indentation in both axial and transverse directions for different material models (see Table 1)

3.3. Strain gradients

Apparently, the indentation process caused considerable non-uniformity in strain distributions. Figure 9(a), (b), (c) demonstrates the distributions of equivalent plastic strains on different paths obtained for indentations in transverse and axial directions for models I and A. It was observed that when a material was indented in transverse direction, an increasing magnitude of AR resulted in change of relative positions of graphs on paths A-B and C-D, with strain gradients being less significant in the former case and more

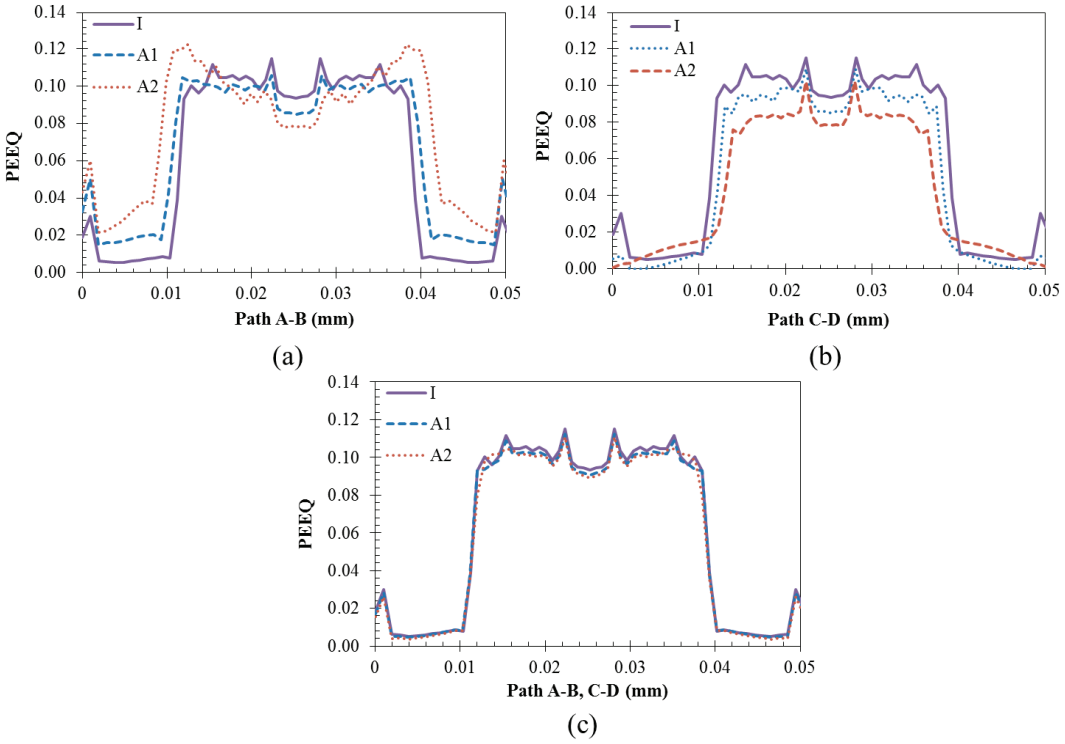

Fig. 9. Distribution of equivalent plastic strains (PEEQ) along paths A-B and C-D (Fig. 5) at maximum loading from indentation in transverse (a, b) and axial directions (c) for models I and A

significant in the latter. On the other hand, a change of AR for axial indentation did not affect the strain distributions substantially.

4. Discussion

It was observed that the slope of the unloading part of the curve was identical for the material model C, but it was changing for models A and B (in indentation along both directions) (Fig. 3). This is due to the fact that as this slope indeed represents the capability of the elastic recovery of the material upon unloading (retraction of the indenter), only the variation in elasticity AR affects the slope of this curve. These observations can also be apprehended from Fig. 4. These values are related to the slope of unloading curves for all the models.

The values of elastic moduli obtained from finite-element simulations of nano-indentation employing material model I (i.e., fully isotropic formulation) were compared with that used as an input. Apparently, in an ideal case these values should be the same; any deviation means an effect of additional factors, e.g., anisotropy, pile-upping, etc. It was observed that using the O-P method, E was found to be 20.28 GPa and 19.16 GPa, when the contact areas $A_{\text{p-OP}}$ and $A_{\text{p-FE}}$ were used in equation (2), leading to overestimation of the input value (18 GPa, Table 2), by 12.7% and 6.5%, respectively. This means that as the O-P method is based on a strictly elastic analysis, which does not account for pile-up, it fails to adequately predict the elastic-modulus values. The results also showed that, even if the accurate contact area was used, accounting for the pile-up obtained, e.g. from FE simulations, still some amount of disparity was observed. The results confirm that plastic deformation in indentation affects the load-displacement curve in such a way that an accurate analysis cannot be achieved by means of the elastic solutions only. Bolshakov and Pharr [4] reported that when the portion of the indenter displacement, which is elastically recovered during unloading, was high, i.e., the ratio of h_{f} to h_{max} was less than 0.7, sink-in occurred around the indent and the O-P method gave comparatively better predictions. In our study, this ratio was approx. 0.9, with a lower extent of elastic recovery.

The underlying reason for the observations in Fig. 6 can be explained in the following way. Depending on the relative amounts of elastic and plastic components in the deformation process, characterized by the ratio of elastic modulus to yield stress, E/σ_Y, the surface either piles-up or sinks-in [24]. Johnson [13] characterized this ratio as the reciprocal of the level of elastic strain at the yield point representing the amount of

deformation accommodated elastically during indentation. For instance, in the limit of $E/\sigma_Y = 0$, deformation is purely elastic leading to a sink-in surface profile, whereas in the limit of $E/\sigma_Y = \infty$, deformation is rigid-plastic, with an extensive piling-up of the material around the indent. Therefore, an increase in the value of *AR* for elasticity in transverse indentation caused the pile-up height to decrease on path A-B (Fig. 6(a)) since the elasticity modulus along the transverse axis became smaller. This resulted in a decreasing pile-up profile on path C-D (Fig. 6(b)). On the other hand, an increase in *AR* for plasticity in transverse indentation resulted in the increased pile-up height on path A-B as yield point related to the transverse axis became smaller (Fig. 6(c)). This resulted in a decreasing pile-up profile on path C-D (Fig. 6(d)). As $A_{\text{p-FE}}$ accounted for the pile-up heights in its calculations, the observations of the effect of different models on the surface profile might be linked to their effect on $A_{\text{p-FE}}$. For instance, an increase in the value of *AR* for elasticity in transverse indentation led $A_{\text{p-FE}}$ to decrease (Table 3) due to the fact that this change lessened the resulting pile-up heights (Fig. 6(a, b)). On the other hand, an increased *AR* for plasticity led to an opposite result, i.e. $A_{\text{p-FE}}$ increased. This result justified that the pile-up height increase on path A-B (Fig. 6(c)) overcompensated the pile-up height decrease on path C-D (Fig. 6(d)) in the $A_{\text{p-FE}}$ obtained.

It is well recognised that indentation hardness of a metallic material at the micron or sub-micron scales is dramatically different from that at macro-scale, known as the size effect. This phenomenon was attributed to the presence of strain gradients associated with non-uniform plastic deformation in small volumes [8], [9], [11]. Hence, the change in the material's *AR* affected the character of strain gradients when indented in the transverse direction. As a result, a different extent of realisation of the size effect should be expected for different models, and a similar one for axial indentation. However, it should be noted that in this study the value of *AR* was changed with keeping the parameters in the longitudinal direction and varying those for the transverse directions; hence, strain gradients become important in the latter compared to the former. Our detailed study on the influence of the model formulation on realisation of the size effect will be reported in the future.

The present model can be used to assess the effect of variation of constitutive parameters such as the anisotropy ratio due to age, sex, injury and/or disease on a deformational behaviour of bone under loading conditions resulting in multi-axial stress fields such as in drilling operations [3], [15], [22]. For this, the present model needs to be enhanced by coupling it thermo-mechanically (since thermal necrosis is a significant concern in such cases) and activating its remeshing module to cope with large deformations in the process zone that causes element distortions in simulations.

Numerical simulations provide a unique opportunity to consider various material formulations, e.g., different extents of anisotropy of elastic and/or post-yield regimes that cannot be achieved in experimental studies. It is especially important, since, though cortical bone is known as an anisotropic material, the nano-indentation approaches used are still mostly based on the isotropic theory. The results of this paper quantify the effect of such oversimplified material formulation on the parameters measured with indentation.

Acknowledgement

The authors acknowledge the financial support from EPSRC UK (grant no. EP/G048886/1).

References

[1] ABDEL-WAHAB A.A., ALAM K., SILBERSCHMIDT V.V., *Analysis of anisotropic viscoelastoplastic properties of cortical bone tissues*, J. Mech. Behav. Biomed. Mater, 2011, 4, 807–820.

[2] ABDEL-WAHAB A.A., SILBERSCHMIDT V.V., *Plastic behaviour of microstructural constituents of cortical bone tissue: A nanoindentation study*, I. J. Exp. Comp. Biomech., 2013, 2, 136–157.

[3] ALAM K., MITROFANOV A.V., SILBERSCHMIDT V.V., *Experimental investigations of forces and torque in conventional and ultrasonically-assisted drilling of cortical bone*, Med. Eng. Phys., 2011, 33, 234–239.

[4] BOLSHAKOV A., PHARR G.M., *Influences of pileup on the measurement of mechanical properties by load and depth sensing indentation techniques*, J. Mater. Res., 1998, 13, 1049–1058.

[5] BUCAILLE J.-L., STAUSS S., FELDER E., MICHLER J., *Determination of plastic properties of metals by instrumented indentation using different sharp indenters*, Acta Mater., 2003, 51, 1663–1678.

[6] CARNELLI D., GASTALDI D., SASSI V., CONTRO R., ORTIZ C., VENA P., A *finite element model for direction-dependent mechanical response to nanoindentation of cortical bone allowing for anisotropic post-yield behavior of the tissue*, J. Biomech. Eng., 2010, 132, 081008–081008.

[7] CARNELLI D., RICCARDO L., MATTEO P., ROBERTO C., PASQUALE V., *Nanoindentation testing and finite element simulations of cortical bone allowing for anisotropic elastic and inelastic mechanical response*, J. Biomech., 2011, 44, 1852–1858.

[8] DEMIRAL M., ROY A., EL SAYED T., SILBERSCHMIDT V., *Influence of strain gradients on lattice rotation in nano-indentation experiments: A numerical study*, Mater. Sci. Eng. A, 2014, 608, 73–81.

[9] DEMIRAL M., ROY A., SILBERSCHMIDT V., *Indentation studies in b.c.c. crystals with enhanced model of strain-gradient crystal plasticity*, Comput. Mater. Sci., 2013, 79, 896–902.

[10] FAN Z., RHO J.Y., SWADENER J.G., PHARR G.M., *Three-dimensional finite element analysis of the effects of anisotropy on bone mechanical properties measured by nanoindentation*, J. Mater. Res., 2004, 19, 114–123.

[11] FLECK N.A., HUTCHINSON J.W., *A reformulation of strain gradient plasticity*, J. Mech. Phys. Solids, 2001, 49, 2245–2271.

[12] HUWALDT J.A., *Plot Digitizer 2.4.1.*, Freeware software distributed from <http://sourceforge.net/projects/plotdigitizer> (verified June 2008), 2005.

[13] JOHNSON K.L., *Contact mechanics*, Cambridge University Press, Cambridge, 1974.

[14] KAN Q., YAN W., KANG G., SUN Q., *Oliver–Pharr indentation method in determining elastic moduli of shape memory alloys – a phase transformable material*, J. Mech. Phys. Solids, 2013, 61, 2015–2033.

[15] KARACA F., AKSAKAL B., *Effects of various drilling parameters on bone during implantology: An in vitro experimental study*, Acta Bioeng. Biomech., 2013, 15, 25–32.

[16] LIU D., WEINER S., WAGNER H.D., *Anisotropic mechanical properties of lamellar bone using miniature cantilever bending specimens*, J. Biomech., 1999, 32, 647–654.

[17] MULLINS L.P., MCGARRY J.P., BRUZZI M.S., MCHUGH P.E., *Micromechanical modelling of cortical bone*, Comp. Methods Biomech. Biomed. Eng., 2007, 10, 159–169.

[18] OLIVER W.C., PHARR G.M., *Measurement of hardness and elastic modulus by instrumented indentation: Advances in understanding and refinements to methodology*, J. Mater. Res., 2004, 19, 3–20.

[19] ÖZKAN A., ATMACA H., MUTLU İ., ÇELIK T., UĞUR L., KIŞIOĞLU Y., *Stress distribution comparisons of foot bones in patient with tibia vara: a finite element study*, Acta Bioeng. Biomech., 2013, 15, 67–72.

[20] REILLY D.T., BURSTEIN A.H., FRANKEL V.H., *The elastic modulus for bone*, J. Biomech., 1974, 7, 271–275.

[21] RHO J.-Y., ROY M.E., TSUI T.Y., PHARR G.M., *Elastic properties of microstructural components of human bone tissue as measured by nanoindentation*, J. Biomed. Mater. Res., 1999, 45, 48–54.

[22] SEZEK S., AKSAKAL B., KARACA F., *Influence of drill parameters on bone temperature and necrosis: A FEM modeling and in vitro experiments*, Comput. Mater. Sci., 2012, 60, 13–18.

[23] Systèmes, Dassault. "Abaqus 6.10: Analysis user's manual". Providence, RI: Dassault Systèmes Simulia Corp, 2010.

[24] TALJAT B., PHARR G.M., *Development of pile-up during spherical indentation of elastic–plastic solids*, I. J. Solids Struct., 2004, 41, 3891–3904.

[25] WANG X.J., CHEN X.B., HODGSON P.D., WEN C.E., *Elastic modulus and hardness of cortical and trabecular bovine bone measured by nano-indentation*, Trans. Nonferr. Metals Soc. China, 2006, 16, 744–748.

[26] WEINER S., ADDADI L., WAGNER H.D., *Materials design in biology*, Mater. Sci. Eng.C, 2000, 11, 1–8.

[27] ZAAFARANI N., RAABE D., SINGH R.N., ROTERS F., ZAEFFERER S., *Three-dimensional investigation of the texture and microstructure below a nanoindent in a Cu single crystal using 3D EBSD and crystal plasticity finite element simulations*, Acta Mater., 2006, 54, 1863–1876.